Improved surface-roughness scattering and mobility models for multi-gate FETs with arbitrary cross-section and biasing scheme

D. Lizzit, O. Badami, R. Specogna, and D. Esseni

Citation: Journal of Applied Physics **121**, 245301 (2017); doi: 10.1063/1.4986644
View online: http://dx.doi.org/10.1063/1.4986644
View Table of Contents: http://aip.scitation.org/toc/jap/121/24
Published by the American Institute of Physics

Improved surface-roughness scattering and mobility models for multi-gate FETs with arbitrary cross-section and biasing scheme

D. Lizzit,[a] O. Badami,[a] R. Specogna, and D. Esseni
DPIA, University of Udine, Via delle Scienze 206, 33100 Udine, Italy

(Received 28 February 2017; accepted 5 June 2017; published online 23 June 2017)

We present a new model for surface roughness (SR) scattering in *n*-type multi-gate FETs (MuGFETs) and gate-all-around nanowire FETs with fairly arbitrary cross-sections, its implementation in a complete device simulator, and the validation against experimental electron mobility data. The model describes the SR scattering matrix elements as non-linear transformations of interface fluctuations, which strongly influences the root mean square value of the roughness required to reproduce experimental mobility data. Mobility simulations are performed via the deterministic solution of the Boltzmann transport equation for a 1D-electron gas and including the most relevant scattering mechanisms for electronic transport, such as acoustic, polar, and non-polar optical phonon scattering, Coulomb scattering, and SR scattering. Simulation results show the importance of accounting for arbitrary cross-sections and biasing conditions when compared to experimental data. We also discuss how mobility is affected by the shape of the cross-section as well as by its area in gate-all-around and tri-gate MuGFETs. *Published by AIP Publishing.* [http://dx.doi.org/10.1063/1.4986644]

I. INTRODUCTION

The aggressive downscaling of CMOS transistors demands for design solutions to obtain large drive currents at small supply voltage and preserve low leakage currents. The possible options for technology improvement include the reduction of source/drain series resistance that is responsible for a degradation of the transistor on-current by 30%–40%,[1,2] the use of semiconductors alternative to silicon,[2–8] the introduction of stressors,[9,10] and the development of device architectures beyond planar FETs such as multi-gate FETs (MuGFETs).[7,9,11] In particular, for CMOS generations beyond the 7-nm node, gate-all-around (GAA) nanowire FETs appear to be the most promising architecture.[1,2,5,12–15] However, nanowire transistors still face significant challenges and, due to the high surface-to-volume ratio, the performance of these devices is strongly influenced by surface roughness (SR) and interface defects.[16–21]

In this framework, an accurate description of interface effects in order to predict the device performance is required, and the aim of this work is to present a new model for SR scattering in MuGFETs with arbitrary cross-sections. The model is based on a non-linear relation between the surface roughness (SR) matrix elements and the random fluctuations of the interface position, and a similar approach has been already developed and demonstrated for planar bulk and UTB MOSFETs,[22,23] as an alternative to the standard Prange-Nee and generalized Prange-Nee models widely used in the literature for planar FETs,[24–38] MuGFETs, and GAA-FETs.[39,40]

The new SR model has been implemented in a complete device simulator, where carrier transport is described by using the deterministic solution of the multi-valley Boltzmann Transport Equation (BTE) with no simplifying approximation, such as momentum relaxation time (MTR)[34,41] or linearization of the BTE.[42] Electrostatics and transport equations are solved for arbitrary device cross-sections and accounting for scattering rates due to phonons, Coulomb scattering, and SR according to the new formulation developed in this paper.

This paper is organized as follows. In Sec. II, we present the quantization model employed for arbitrary shaped cross-sections and the non-parabolicity corrections to the energy relation. Then, in Sec. III we illustrate the new SR scattering model and discuss some well justified approximations useful to decrease the computational burden of SR scattering calculations. Some additional, important physical ingredients of our transport model are briefly discussed in Sec. IV, such as phonon and Coulomb scattering as well as the screening produced by free carriers, while in Sec. V, we concisely illustrate the deterministic solution of the BTE. Section VI shows a validation of our mobility calculations against previous simulation results; then, we compare our simulations with mobility experimental data and finally investigate the influence of the cross-sectional shape and area on the electron mobility of nanowire FETs. Some concluding remarks are proposed in Sec. VII.

II. CONFINED ELECTRON GAS IN ARBITRARY CROSS-SECTION MuGFET

The electron envelope wave-function for the 1D electron gas (1DEG) is written as

$$\Psi_{n,k_x}(\mathbf{r},x) = \xi_n(\mathbf{r})\frac{e^{ik_x x}}{\sqrt{L_x}}, \tag{1}$$

where L_x is the normalization length in the transport direction, $k_x = n(2\pi/L_x)$ (with $n = 0, \pm1, \pm2,\ldots$), and $\mathbf{r} = (y, z)$ is the position in the section of the wire, as illustrated in the sketch of Fig. 1. The envelope wave-function $\xi_n(\mathbf{r})$ is obtained by solving the Schrödinger equation corresponding to the parabolic effective mass approximation

[a]D. Lizzit and O. Badami contributed equally to this work.

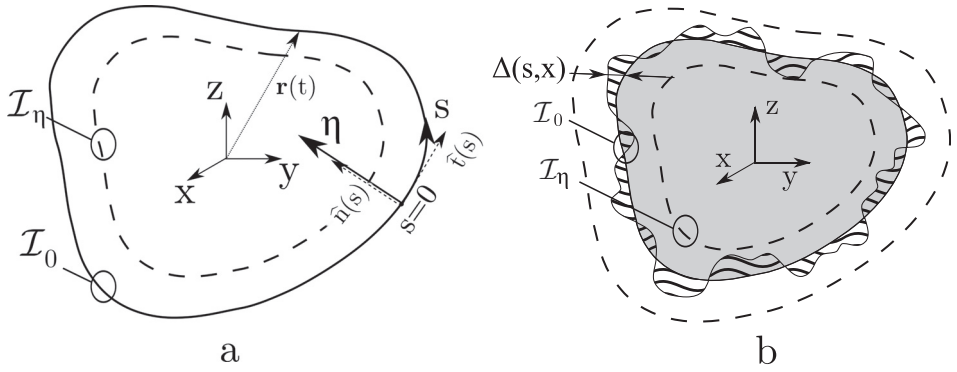

FIG. 1. (a) Sketch of the cross-section of a MuGFET where x is the transport direction and $\mathcal{I}_0$ denotes the curve describing the semiconductor-oxide interface. s and η are, respectively, the abscissa along $\mathcal{I}_0$ and normal to $\mathcal{I}_0$, and $\mathcal{I}_\eta$ is the curve at a distance η from $\mathcal{I}_0$. D_0 and D_η are the lengths of the perimeters $\mathcal{I}_0$ (i.e., the perimeter of the semiconductor region) and $\mathcal{I}_\eta$. (b) sketch of the cross-section of a MuGFET perturbed by a surface roughness stochastic process $\Delta(s, x)$. The dashed area is the perturbed region P_R $[\Delta(s, x)]$ where $\Delta(s, x)$ is non null; the grey region is the semiconductor.

$$\left[-\frac{\hbar^2}{2}\nabla\cdot(\mathbf{W}_{yz}\nabla)+U(\mathbf{r})\right]\xi_n(\mathbf{r})=\varepsilon_n^{(p)}\xi_n(\mathbf{r}), \tag{2}$$

where $\mathbf{W}_{yz}$ is the 2×2 matrix of the inverse effective masses in the device coordinate system defined as

$$\mathbf{W}_{yz}=\begin{pmatrix} w_{yy} & w_{yz} \\ w_{zy} & w_{zz}\end{pmatrix}, \tag{3}$$

and it is linked to the effective masses of the bulk crystal through appropriate linear transformations.[35] To solve Eq. (2), we used the Discrete Geometric Approach (DGA),[43] which is very effective to describe fairly arbitrary cross-sections (see Fig. 1).

In the DGA, physical variables are defined as fluxes or circulations on oriented geometric elements of a pair of dual interlocked meshes, while physical laws are expressed in a metric-free fashion with incidence matrices. The metric and the material information are encoded in the discrete counterpart of the constitutive laws of materials, also referred to as material matrices or discrete Hodge operators.[44] The stability and consistency of the method are guaranteed by precise properties (symmetry, positive definiteness, and geometric consistency) that material matrices have to fulfill. The main advantage of DGA is that material matrices, even for arbitrary star-shaped polyhedral elements, can be geometrically defined by simple closed-form expressions in terms of the geometric elements of the primal and dual meshes. Moreover, when DGA is applied to the stationary Schrödinger problem, a second order convergence of eigenvalues is obtained by solving a standard eigenvalue problem,[43,44] whereas the corresponding Finite Element formulation requires to solve a generalized eigenvalue problem which is much more computationally demanding.

The electron band structure in the conduction band is calculated using the non-parabolic effective mass approximation model (EMA-NP);[34] in fact, the non-parabolicity may play an important role in both subband splitting and transport, particularly for III-V based transistors.[45–47] Non-parabolicity effects in the quantization plane (y, z) and transport direction (x) are described writing the energy as[34]

$$E_n=\langle U_n\rangle+\frac{\sqrt{1+4\alpha\left[\frac{\hbar^2}{2}\frac{k_x^2}{m_x}+\varepsilon_n^{(p)}-\langle U_n\rangle\right]}-1}{2\alpha}, \tag{4}$$

where $\langle U_n\rangle=\int_y\int_z|\xi_n(y,z)|^2\,U(y,z)\,dy\,dz$ is the expectation value of the potential energy $U(y, z)$ in the device section, and α is the non-parabolicity factor. Relevant effective masses and α values for Si and InAs are reported in Table I. Moreover, $\varepsilon_n^{(p)}$ and $\xi_n(y, z)$ are, respectively, subband minima and wave-functions for the parabolic effective mass Hamiltonian in Eq. (2).

The Schrödinger solver accounts for multi-valley systems, for anisotropic effective masses in the (y, z) plane (i.e., no isotropic approximations), and for the wave-function penetration in the oxide region,[48] which is important for surface roughness scattering modeling. Continuity conditions for $\xi_n(\mathbf{r})$ and $\mathbf{W}_{yz}\nabla\xi_n(\mathbf{r})$ (where $\nabla(\cdot)$ is the gradient operator) are implicitly satisfied by the DGA method at the semiconductor-oxide interface.

We here notice that, in the case of cylindrical nanowires, it is convenient to solve Eq. (2) by using polar coordinates (r, θ). Then, one can take advantage of the fact that $\xi_n(r, \theta)$ is periodic in θ (at any r), and use a Fourier series expansion to write

$$\xi_n(r,\theta)=\sum_l \rho_{nl}(r)e^{il\theta}\quad l=0,\pm1,\pm2,\ldots \tag{5}$$

where $\rho_{nl}(r)$ is defined as

TABLE I. Bulk effective mass, non-parabolicity coefficient α, and electron affinity χ for InAs and Si. The energy difference between the L and Γ conduction band minima in InAs is set to 0.716 eV.[69]

		Effective mass			
Material	Valley	m_l (m_0)	m_t (m_0)	α (eV^{-1})	χ (eV)
InAs	Γ[70]	0.026	0.026	2.5	4.9
	L[71]	1.565	0.124	0.45	
Si	Δ[35]	0.916	0.19	0.5	4.05

$$\rho_{nl}(r) = \frac{1}{2\pi}\int_{-\pi}^{+\pi} \xi_n(r,\theta)e^{-il\theta}\,d\theta, \tag{6}$$

and $\rho_{n(-l)}(r) = \rho^{\dagger}_{nl}(r)$ because $\xi_n(\mathbf{r})$ is a real valued function. It should be noticed that l in Eq. (6) is *not* an angular quantization number; in fact, Eq. (2) does not allow one to identify an angular quantum number except for the isotropic case, which corresponds to $w_{yy} = w_{zz}$ and $w_{yz} = w_{zy} = 0$ in Eq. (3). Equation (5) will be particularly useful in the treatment of Coulomb scattering matrix elements and carrier screening in cylindrical nanowires, as discussed below in Sec. IV.

III. MODELING OF SURFACE ROUGHNESS SCATTERING

Surface roughness (SR) scattering in ultra-scaled transistors is a dominant scattering mechanism, which limits the carrier mobility especially at large inversion densities.[30,34,49–51] In the literature, several SR models have been reported even for 3D FETs with arbitrary cross-sections;[39,52,53] however, all models assume that matrix elements are simply proportional to $\Delta(\mathbf{r}_I)$, where $\Delta(\mathbf{r}_I)$ is the random fluctuation of the interface position versus the abscissa $\mathbf{r}_I$ at the semiconductor-oxide interface. As demonstrated for planar transistors,[22] however, SR matrix elements exhibit instead a quite strong nonlinear dependence on $\Delta(\mathbf{r}_I)$, so that in this paper we extend to MuGFET and nanowire MOSFETs the non-linear model for SR scattering that we recently proposed for planar transistors.[22] Figure 1(b) shows an arbitrary device cross-section where $\mathcal{I}_0$ is the curve describing the nominal, unperturbed semiconductor-oxide interface in the cross-section, with s and η being the abscissa, respectively, along $\mathcal{I}_0$ and normal to $\mathcal{I}_0$. In a cylindrical nanowire, for example, η is the radial direction and s is the abscissa along the circumference. Surface roughness is a stochastic process describing the fluctuations $\Delta(s, x)$ of the interface position at each point $\mathbf{r}_I = (s, x)$ of the unperturbed interface. $\mathrm{P_R}[\Delta(s, x)]$ denotes the perturbed region that is the narrow region close to $\mathcal{I}_0$ illustrated in Fig. 1(b), which contributes to SR matrix elements because $\Delta(s, x)$ is non-null. By following Ref. 22, we now write the SR matrix element as

$$\mathcal{M}_n^{n'}(q_x) = \frac{1}{L_x}\int_{L_x}\left[\iint_{\mathrm{P_R}[\Delta(s,x)]} \xi^{\dagger}_{n'}(\mathbf{r})\,\Phi_B\,\xi_n(\mathbf{r})\,d\mathbf{r}\right]e^{-iq_x x}\,dx, \tag{7}$$

where $q_x = k_x^{'} - k_x$ is the exchanged wave-vector and Φ_B is the semiconductor-oxide energy barrier. As it can be seen, Eq. (7) neglects the kinetic energy contribution to the matrix element because, as discussed in detail for planar transistors,[22] the kinetic energy term can lead to unphysically large matrix elements when using the EMA energy model; a more accurate description of the kinetic energy contribution may be obtained using a Hamiltonian going beyond the EMA model,[54] but this problem is outside the scope of the present work.

Since SR is a stochastic process occurring at the interface $\mathcal{I}_0$ and it is thus a function of (s, x), we now intend to write $\xi_n(\mathbf{r})$ by using the curvilinear coordinates (s, η) sketched in Fig. 1. Figure 1(a) shows that η is the abscissa normal to $\mathcal{I}_0$ at each point s along $\mathcal{I}_0$ and that $\mathcal{I}_\eta$ is the curve of length D_η obtained by moving a distance η in the direction normal to $\mathcal{I}_0$ identified by the unit vector $\hat{n}(s)$.

Since $\xi_n(\mathbf{r})$ is periodic in the abscissa s_η along each curve $\mathcal{I}_\eta$, we can use Fourier series and write

$$\xi_n(s_\eta, \eta) = \sum_l \phi_{n,l}(\eta)e^{i2\pi l s_\eta/D_\eta} \quad l = 0, \pm1, \pm2, \ldots \tag{8}$$

with $\phi_{n,l}(\eta)$ defined as

$$\phi_{n,l}(\eta) = \frac{1}{D_\eta}\int_{\mathcal{I}_\eta} \xi_n(\mathbf{r})e^{-i2\pi l s_\eta/D_\eta}\,d\mathbf{r}\,. \tag{9}$$

Equation (9) allows one to determine the coefficients $\phi_{n,l}(\eta)$ from the $\xi_n(\mathbf{r})$ obtained by the Schrödinger solver by means of a numerical integration over the curve $\mathcal{I}_\eta$.

By substituting Eq. (8) into Eq. (7) and following Appendix A, we can write the matrix element in curvilinear coordinates as

$$\mathcal{M}_n^{n'}(q_x) = \frac{1}{L_x D_0}\sum_{l,l'}\int_{L_x}\left[\int_{D_0} M_{nl}^{n'l'}\left[\Delta(s,x)\right]\,e^{-iq_{ll'}s}ds\right]e^{-iq_x x}dx, \tag{10}$$

where $M_{nl}^{n'l'}[\Delta(s,x)]$ is defined as

$$M_{nl}^{n'l'}[\Delta(s,x)] = \int_0^{\Delta(s,x)} D_\eta\,\phi^{\dagger}_{n'l'}(\eta)\,\Phi_B\,\phi_{nl}(\eta)\,d\eta, \tag{11}$$

and $q_{ll'} = 2\pi(l' - l)/D_0$. Figure 1(a) shows that for $\Delta > 0$ the interface enters the semiconductor region and for $\Delta < 0$ the interface sets back into the oxide region.

The wave-function $\xi_n(\mathbf{r})$ is strongly asymmetric across the semiconductor-oxide interface as shown in Fig. 2(a); in fact, it has approximately sinusoidal features in the semiconductor, whereas it decays exponentially in the oxide region. Consequently, $M_{nl}^{n'l'}$ defined in Eq. (11) is a markedly nonlinear function of Δ as shown in Fig. 2(b), and $M_{nl}^{n'l'}[\Delta(s,x)]$ is thus a nonlinear transformation of the random process $\Delta(s, x)$.[22] The ensemble averaged squared matrix element is given by definition as

$$\langle|\mathcal{M}_n^{n'}(q_x)|^2\rangle = \frac{1}{(L_x D_0)^2}\sum_{\substack{l,l'\\g,g'}}\int_{L_x}\int_{L_x} dx\,dx'\int_{D_0}\int_{D_0} ds\,ds' e^{-iq_{ll'}s} e^{+iq_{gg'}s'} C_{n,lg}^{n',l'g'}(\boldsymbol{\tau})e^{-iq_x(x-x')}, \tag{12}$$

where $\boldsymbol{\tau} = (s - s', x - x')$ and $C_{n,lg}^{n',l'g'}(\boldsymbol{\tau})$ is defined as

$$C_{n,lg}^{n',l'g'}(\boldsymbol{\tau}) = \langle M_{nl}^{n'l'}[\Delta(s,x)](M_{ng}^{n'g'}\left[\Delta(s',x')\right])^{\dagger}\rangle, \tag{13}$$

with (l, g) and (l', g') being the indexes of the Fourier modes of respectively ξ_n and $\xi_{n'}$ defined in Eqs. (8) and (9). $C_{n,lg}^{n',l'g'}(\boldsymbol{\tau})$ is the cross-correlation function between the matrix elements $M_{nl}^{n'l'}[\Delta(s,x)]$ and $M_{ng}^{n'g'}[\Delta(s',x')]$ and can be written by using the Wiener-Kinchin theorem as the inverse Fourier transform of the power spectrum

$$C_{n,lg}^{n',l'g'}(\boldsymbol{\tau}) = \frac{1}{(2\pi)^2}\int_{q_s} dq_s \int_{q_{x'}} dq_x' S_{n,lg}^{n',l'g'}(q_s, q_x')e^{iq_s(s-s')}e^{iq_x'(x-x')}, \tag{14}$$

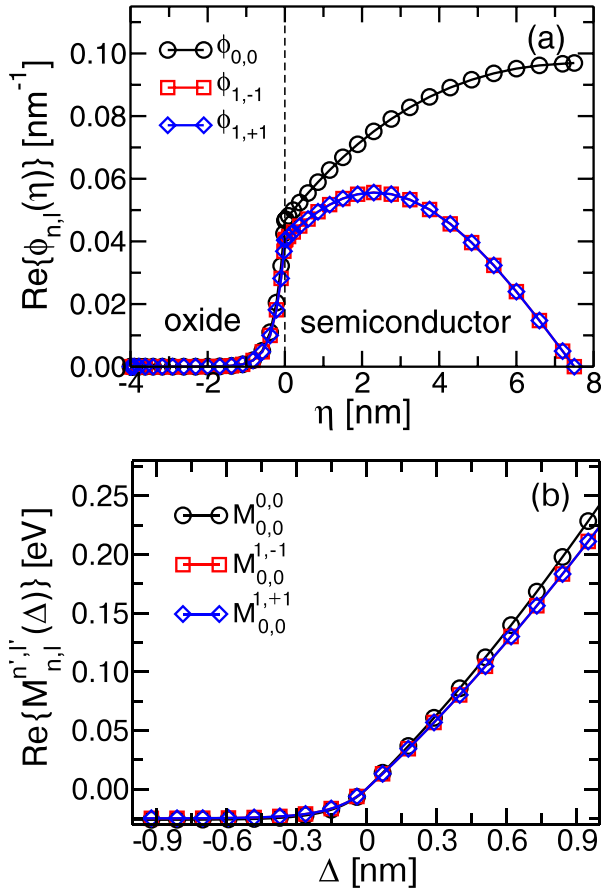

FIG. 2. ZrO_2-InAs circular GAA nanowire with oxide thickness of 4 nm and semiconductor diameter d = 15 nm. (a) Real part of the terms $\phi_{n,l}$ along η for the lowest subband (n = 0) and for n = 1 and defined by Eq. (9). (b) Real part of the SR matrix element versus Δ computed by means of Eq. (11) using the $\phi_{n,l}$ terms shown in figure (a).

where $S^{n',l'g'}_{n,lg}(q_s,q'_x)$ is the cross-correlation power spectrum of $M^{n'l'}_{nl}[\Delta(s,x)]$ and $M^{n'g'}_{ng}[\Delta(s',x')]$; an explicit expression for $S^{n',l'g'}_{n,lg}(q_s,q'_x)$ will be discussed below. Equation (14) has been written for a continuous q_x, which implies a large normalization length along the x direction; Eq. (14) also assumes that the length D_0 of the perimeter of the interface $\mathcal{I}_0$ in the device cross-section is much larger than the correlation length Λ of the $\Delta(s,\ x)$ process, which is a very reasonable approximation for most devices of practical interests and for a Λ in the range of 1 to 2 nm.

We now complete the derivations for $\langle|\mathcal{M}^{n'}_n(q_x)|^2\rangle$ by substituting Eq. (14) into Eq. (12) and obtain

$$\langle|\mathcal{M}^{n'}_n(q_x)|^2\rangle = \frac{1}{(2\pi L_x D_0)^2}\sum_{\substack{l,l'\\g,g'}}\int_{q_s}dq_s\int_{q'_x}dq'_x\,S^{n',l'g'}_{n,lg}(q_s,q'_x)\times\int_{L_x}\int dx\,dx'\,e^{i(q'_x-q_x)(x-x')}\times\int_{D_0}ds\,e^{-i(q_{ll'}-q_s)s}\int_{D_0}ds'\,e^{+i(q_{gg'}-q_s)s'}. \quad (15)$$

The integrals over x, x' and s, s' can be evaluated analytically. For a large L_x, we have

$$\lim_{L_x\to\infty}\int_{L_x}\int e^{i(q'_x-q_x)(x-x')}dx\,dx' = 2\pi L_x\delta(q'_x-q_x), \quad (16)$$

while for integrals over s we have

$$\frac{1}{D_0}\int_{D_0}e^{iqs}ds = \frac{\sin(0.5\,D_0\,q)}{0.5\,D_0\,q} \equiv \mathrm{sinc}(0.5\,D_0\,q). \quad (17)$$

By substituting Eqs. (16) and (17) into Eq. (15) and noting that $\delta(q'_x-q_x)$ reduces the integral over q'_x, Eq. (15) can be cast into the compact form

$$\langle|\mathcal{M}^{n'}_n(q_x)|^2\rangle = \frac{1}{L_x D_0}\sum_{\substack{l,l'\\g,g'}}\int_{q_s}dq_s\,F(q_{ll'},q_{gg'},q_s)S^{n',l'g'}_{n,lg}(q_s,q_x), \quad (18)$$

where the form factor is defined as

$$F(q_{ll'},q_{gg'},q_s) = \frac{D_0}{2\pi}\mathrm{sinc}\left[\frac{(q_{ll'}-q_s)D_0}{2}\right]\mathrm{sinc}\left[\frac{(q_{gg'}-q_s)D_0}{2}\right]. \quad (19)$$

It is readily seen that for $q_{ll'} = q_{gg'}$ we have

$$\int_{q_s}F(q_{ll'},q_{ll'},q_s)\,dq_s = 1, \quad (20)$$

and that, for a large D_0 of the curve $\mathcal{I}_0$ at the semiconductor-oxide interface, $F(q_{ll'},q_{ll'},q_s)$ tends to the Dirac function, that is, $\lim_{D_0\to\infty}F(q_{ll'},q_{ll'},q_s) = \delta(q_{ll'}-q_s)$.

For the calculation of the cross-correlation power spectrum $S^{n',l'g'}_{n,lg}(q_s,q_x)$ in Eq. (18), we first need an explicit expression for the cross-correlation function $C^{n',l'g'}_{n,lg}(\tau)$, which we write as[23,55]

$$C^{n',l'g'}_{n,lg}(\tau) = \frac{1}{2\pi\,C_\Delta(0)\sqrt{1-C^2_{\Delta,N}(\tau)}}\times\int_{-\infty}^{+\infty}\int_{-\infty}^{+\infty}M^{n'l'}_{nl}[\Delta_1]\left(M^{n'g'}_{ng}[\Delta_2]\right)^\dagger\times\exp\left[-\frac{\Delta_1^2+\Delta_2^2-2C_{\Delta,N}(\tau)\Delta_1\Delta_2}{2C_\Delta(0)\left(1-C^2_{\Delta,N}(\tau)\right)}\right]d\Delta_1\,d\Delta_2, \quad (21)$$

where $C_\Delta(\tau)$ is the auto-correlation function of the roughness process itself, $\Delta(s,x)$, and $C_{\Delta,N}(\tau) = C_\Delta(\tau)/C_\Delta(0)$. In this work, we employ an exponential correlation function for the roughness,[26] $C_\Delta(\tau) = \Delta^2_{rms}e^{-\tau\sqrt{2}/\Lambda}$; therefore, $C^{n',l'g'}_{n,lg}(\tau)$ depends only on $\tau = |\boldsymbol{\tau}|$ (with $\boldsymbol{\tau} = (s-s', x-x')$) and the power spectrum to be used in Eq. (18) can be finally expressed as[22]

$$S^{n',l'g'}_{n,lg}(q) = 2\pi\int_0^\infty\tau\,C^{n',l'g'}_{n,lg}(\tau)J_0(q\tau)d\tau, \quad (22)$$

where $J_0(x)$ is the zero order Bessel function.

Equation (18) is the final form for the ensemble averaged, squared matrix element, and we now discuss two simplified expressions for Eq. (18) that allow one for a significant reduction of computational time. In this respect, we first notice that the form factor in Eq. (19) is given by the product of two *sinc*-functions peaked at $q_s = q_{ll'}$ and $q_s = q_{gg'}$, respectively; hence, $F(q_{ll'}, q_{gg'}, q_s)$ for $q_{ll'} \neq q_{gg'}$ is expected to be small compared to $F(q_{ll'}, q_{ll'}, q_s)$. Figure 3 shows examples of form factors for two different lengths D_0 of the perimeter. The form factor for $q_{ll'} = q_{gg'}$ (i.e., for $(l - l') = (g - g')$) is the dominant one and, as expected, by increasing the length of the perimeter $F(q_{ll'}, q_{ll'}, q_s)$ approaches the Dirac function $\delta(q_{ll'} - q_s)$. These features of the form factors suggest two simplified formulations for $\langle|\mathcal{M}_n^{n'}(q_x)|^2\rangle$. The first simplification is obtained by dropping in Eq. (18) the terms with $q_{ll'} \neq q_{gg'}$ and leads to

$$\langle|\mathcal{M}_n^{n'}(q_x)|^2\rangle \approx \frac{1}{L_x D_0} \sum_{(l-l')=(g-g')} \int_{q_s} dq_s F(q_{ll'}, q_{ll'}, q_s) \times S_{n,lg}^{n',l'g'}(q_s, q_x). \quad (23)$$

Then, Eq. (23) can be further simplified by assuming that $F(q_{ll'}, q_{ll'}, q_s) \approx \delta(q_{ll'} - q_s)$ reduces the integral over q_s leading to

$$\langle|\mathcal{M}_n^{n'}(q_x)|^2\rangle = \frac{1}{L_x D_0} \sum_{(l'-l)=(g'-g)} S_{n,lg}^{n',l'g'}(q_{ll'}, q_x). \quad (24)$$

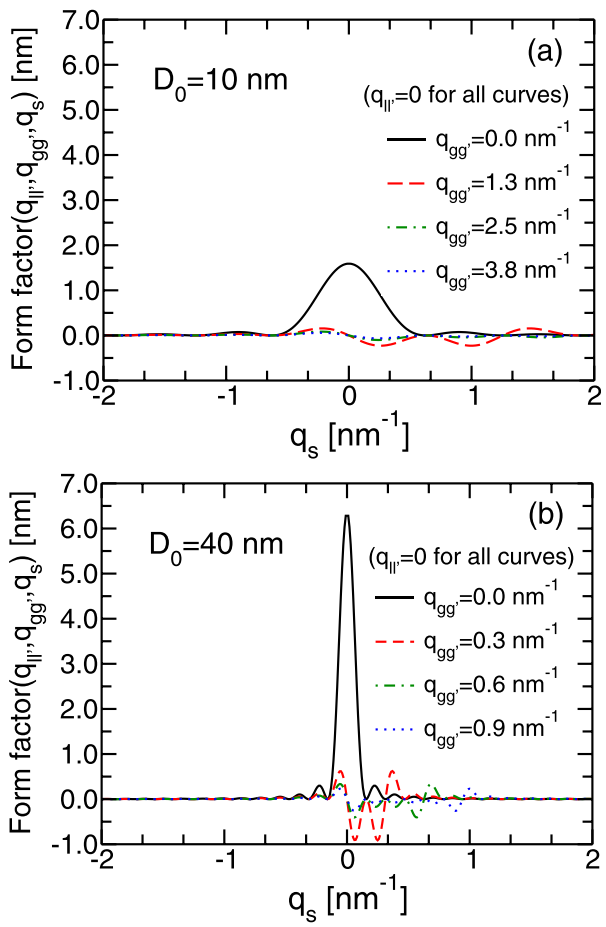

FIG. 3. Form factors obtained from Eq. (19) for $D_0 = 10$ nm (a) and $D_0 = 40$ nm (b). The $q_{gg'} = 2\pi(g' - g)/D_0$ values are obtained by setting $g = 0$ and $g' = 0, 2, 4, 6$.

Figure 4 compares $\langle|\mathcal{M}_n^{n'}(q_x)|^2\rangle$ calculations for a cylindrical silicon nanowire with different transport directions and for a [100] InAs nanowire with different diameters. As can be seen, even Eq. (24) is a very good approximation of Eq. (18), and it can thus be used to obtain an almost 10× reduction of the computational burden. To further validate the approximated expressions for the SR squared matrix elements, Fig. 5 reports mobility calculations for a GAA FET with triangular cross-section and for a Tri-Gate FinFET obtained by using the complete expression in Eq. (18) and the approximated versions given by Eqs. (23) and (24). The figure shows a good agreement between the different formulations over a wide range of inversion carrier densities, N_{inv}.

Another important aspect concerning the computational burden is the number of Fourier modes, l, that must be retained in the calculations. A systematic analysis carried out in this work has shown that for an accurate evaluation of $\langle|\mathcal{M}_n^{n'}(q_x)|^2\rangle$ it is sufficient to consider up to $|l| = 5$ for all the device cross-sections considered herein. This is consistent with the previous assessment reported in Ref. 56.

IV. ADDITIONAL SCATTERING MECHANISMS AND CARRIER SCREENING

Scattering with acoustic, polar, and non-polar optical phonons (POP) and Coulomb scattering have been included in the simulations of this work, and we also accounted for the effects of the screening produced by free carriers. A brief discussion about the corresponding physical models is given in this section.

A. Phonon and Coulomb scattering

Scattering rates for the acoustic intra-valley and optical inter-valley phonon scattering are included with a formulation consistent with Refs. 40 and 57. Optical phonon scattering can assist intra- and inter-valley transitions between subbands belonging to different valleys, where the final valleys and their multiplicity depend on appropriate selection rules.[58]

In polar semiconductors, such as InAs and other III-V materials, the dominant phonon scattering mechanism at room temperature is due to polar optical phonons (POP).[59,60] POP are here included by using a conventional, bulk semiconductor expression for the scattering potential,[59] and the expression for scattering rates is consistent with Ref. 61.

Coulomb scattering has been included in our simulations only for cylindrical nanowires. The squared matrix element for Coulomb scattering is given by[34,35]

$$|\mathcal{M}_{n,n'}(q_x)|^2 = \frac{1}{L_x}\left\{\int_0^\infty dr_0 \int_{-\pi}^{\pi} d\theta_0 r_0 N_{II}(r_0,\theta_0)|\mathcal{M}_{n,n'}^0(q_x,r_0,\theta_0)|^2 + \int_{-\pi}^{\pi} d\theta_0 r_{NW} N_{it}(\theta_0)|\mathcal{M}_{n,n'}^0(q_x,r_{NW},\theta_0)|^2\right\}, \quad (25)$$

where N_{II} denotes a volumetric charge (e.g., due to ionized dopants) and N_{it} denotes a sheet charge at the cylindrical interface (e.g., due to interface states). By recalling the form

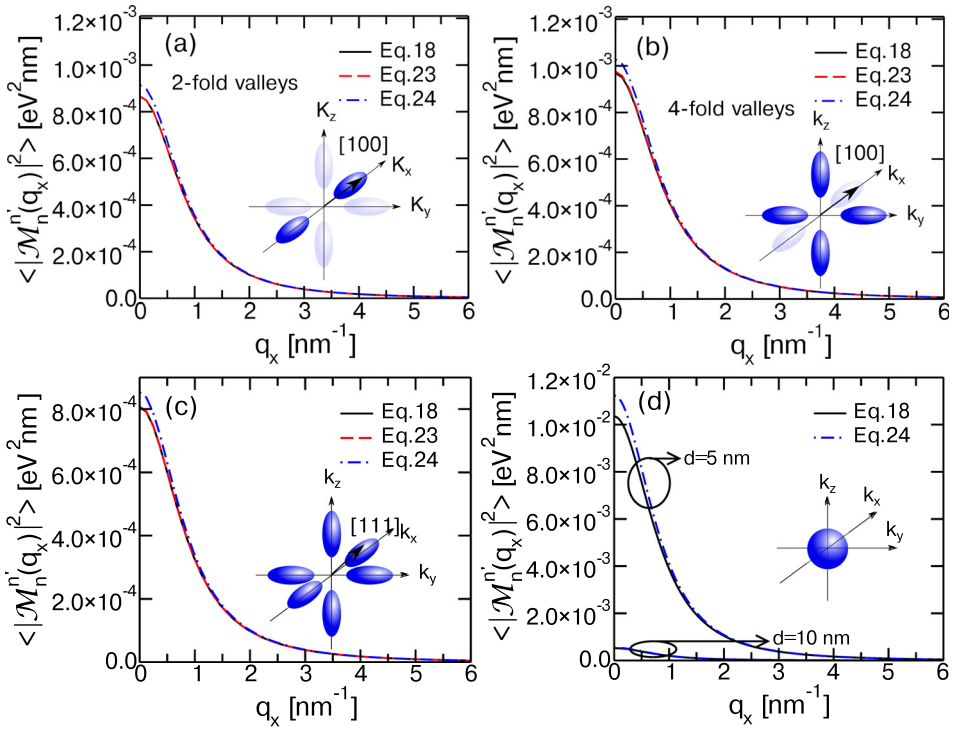

FIG. 4. Intra-subband surface roughness matrix element for the lowest subband (i.e., $n = n' = 0$) in a cylindrical nanowire calculated with its complete form [Eq. (18)], or with approximated expressions in Eqs. (23) and (24). (a), (c), and (b) are for the Si-SiO_2 system with a cross-sectional area of about 40 nm^2 (diameter $d = 7.14$ nm), and inversion density $N_{inv} = 1 \times 10^{13}$ cm^{-2}. (d) is for the InAs-HfO_2 system with diameter $d = 5$ or 10 nm, and $N_{inv} = 5 \times 10^{12}$ cm^{-2}. Results are shown for: (a) [100] transport, two-times degenerate Δ-valleys (see inset); (b) [100] transport, four-times degenerate Δ-valleys; (c) [111] transport, six-times degenerate Δ-valleys; and (d) [100] transport, Γ valley. The parameters of the surface roughness spectrum are $\Delta_{rms} = 0.21$ nm and correlation length $\Lambda = 1.4$ nm. Calculations obtained with Fourier modes up to $|l|, |l|' = 4$. Reprinted with permission from Badami *et al.*, Tech. Dig. - IEEE Int. Electron Devices Meet. 2016, 36.1.1–36.1.4. Copyright 2017 IEEE.[56]

of the wave-function for cylindrical nanowires in Eq. (5), the term $\mathcal{M}^0_{n,n'}(q_x, r_0, \theta_0)$ is given by

$$\mathcal{M}^0_{n,n'}(q_x, r_0, \theta_0) = \frac{e}{\varepsilon_{sct}} \sum_{l,l'} e^{-i(l-l')\theta_0} \int_0^\infty r\, G_{l-l',q_x}(r, r_0) \times \rho_{nl}(r) \rho^\dagger_{n'l'}(r)\, dr, \quad (26)$$

where $G_{l-l',q_x}(r, r_0)$ is the reduced Green's function for the point charge. Exploiting the cylindrical symmetry of the nanowire FET and assuming that all quantities are periodic along the transport direction x over a length L_x, analytical expressions for $G_{l-l',q_x}(r, r_0)$ have been reported in Ref. 34.

B. Carrier screening

The screening produced by the 1D electron gas on a static perturbation potential (e.g., Coulomb or SR scattering potential) is here described by the static dielectric matrix, $\epsilon^{\nu,n,n'}_{w,m,m'}(q_x)$, which allows one to calculate the screened matrix elements $M^{scr}_{\nu,n,n'}(q_x)$, from unscreened matrix elements $M_{w,m,m'}(q_x)$ by solving the linear problem

$$M_{w,m,m'}(q_x) = \sum_{\nu,n,n'} \epsilon^{\nu,n,n'}_{w,m,m'}(q_x) M^{scr}_{\nu,n,n'}(q_x), \quad (27)$$

where (ν, w) are valley indexes and (n, m, n', m') are subband indexes. For a 1D electron gas, the dielectric matrix is

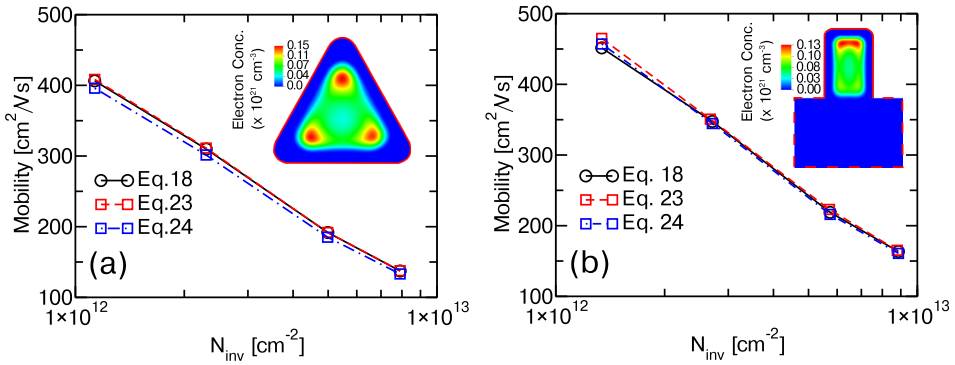

FIG. 5. Simulated electron mobility for a Si-SiO_2 system and for: (a) GAA FET with triangular cross-section, (b) FinFET with aspect ratio H_{fin}/W_{fin} of 2:1. Results are obtained accounting for phonon scattering and SR scattering either with the complete formulation for the matrix elements in Eq. (18) or with approximated expressions in Eqs. (23) and (24). The area is 40 nm^2 and the oxide thickness is 1 nm. Transport direction is [100]. The insets show the electron concentration in the cross-section of each device for the largest N_{inv} of approximately 1×10^{13} cm^{-2}.

written as in Ref. 34, and the expression for the form factor consistent with the wave-function $\xi_n(r, \theta)$ in Eq. (5) is given by

$$F^{\nu,n,n'}_{w,m,m'}(q_x) = 2\pi \sum_{(l-l')=(g-g')} \int_0^\infty r\, dr\, \rho_{w,m,g}(r)\rho^{\dagger}_{w,m',g'}(r) \times \int_0^\infty r_0\, dr_0\, \rho^{\dagger}_{\nu,n,l}(r_0)\, G_{l'-l,q_x}(r, r_0)\, \rho_{\nu,n',l'}(r_0), \tag{28}$$

where (l, l') are Fourier modes of, respectively, ξ_n and $\xi_{n'}$, (g, g') are modes of, respectively, ξ_m and $\xi_{m'}$, while the expressions for the reduced Green's function $G_{l,q}(r, r_0)$ are given in Ref. 34. Equation (27) can be directly used for the screening in Coulomb scattering.

The screening for a linear formulation of the SR scattering is also described directly by Eq. (27) and it has been discussed in several previous contributions.[35] A more complicated formulation for the screening is instead required for the case of the nonlinear SR model of this work, and it is given by[23]

$$\langle|\mathcal{M}^{scr}_{\nu,n,n'}(q_x)|^2\rangle = \sum_{w,m,m'} |L^{\nu,n,n'}_{w,m,m'}(q_x)|^2 \langle|\mathcal{M}^{uns}_{w,m,m'}(q_x)|^2\rangle + \sum_{(w,m,m')\neq(u,p,p')} L^{\nu,n,n'}_{w,m,m'}(q_x) L^{\nu,n,n'}_{u,p,p'}(q_x)^{\dagger} \times \langle \mathcal{M}^{uns}_{w,m,m'}(q_x)(\mathcal{M}^{uns}_{u,p,p'}(q_x))^{\dagger}\rangle, \tag{29}$$

where $L^{\nu,n,n'}_{w,m,m'}(q_x)$ is the inverse of the dielectric matrix $\epsilon^{\nu,n,n'}_{w,m,m'}(q_x)$ and $\langle \mathcal{M}^{uns}_{w,m,m'}(q_x)(\mathcal{M}^{uns}_{u,p,p'}(q_x))^{\dagger}\rangle$ is the cross-correlation power spectrum between the matrix elements $\mathcal{M}^{uns}_{w,m,m'}(q_x)$ and $\mathcal{M}^{uns}_{u,p,p'}(q_x)$, which can be calculated as in Eq. (22) but using the cross-correlation function between $\mathcal{M}^{w,m',l'}_{w,m,l}[\Delta(s,x)]$ and $\mathcal{M}^{u,p',g'}_{u,p,g}[\Delta(s,x)]$.[23] Equation (29) is the screening formulation for SR scattering used throughout this work.

V. MOBILITY CALCULATIONS

In this work, the electron transport (along x direction) is described by a direct, deterministic solution of the Boltzmann transport equation (BTE), with no *a priori* simplifying assumptions about the occupation function $f(x, k_x)$.

The BTE for a 1DEG has been solved using the approach proposed in Ref. 62, which allows us to write the BTE as two ordinary differential equations

$$+|v_{g,n}(x, E_n)|\frac{df^{+}_n(x, E_n)}{dx} = S^{in,+}_n - S^{out,+}_n, \tag{30a}$$

$$-|v_{g,n}(x, E_n)|\frac{df^{-}_n(x, E_n)}{dx} = S^{in,-}_n - S^{out,-}_n, \tag{30b}$$

where $v_{g,n}$ is the group velocity, $S^{in/out,\pm}_n$ are the in- and out-scattering integrals, E_n is the electron energy in subband n given by Eq. (4), and the unknown functions $f^{\pm}_n(x, E_n)$ are defined as

$$f^{+}_n(x, E_n) = f_n(x, k_x), \quad \text{for } k_x > 0, \tag{31a}$$

$$f^{-}_n(x, E_n) = f_n(x, k_x), \text{ for } k_x < 0. \tag{31b}$$

E_n is therefore a parameter in Eq. (30) that must be solved for all the E_n values of interest.

In this work, we do not introduce any approximation for the scattering integrals in the right-hand-side of Eq. (30), such as the momentum relaxation time employed in a number of previous studies.[34,39]

Mobility simulations correspond to a uniform transport regime and a very small lateral electric field F. The solution of the BTE is obtained by discretizing the (x, E_n) with a constant grid spacing and, as illustrated in Fig. 6, for a constant electric field F the unknown occupation functions belonging to different sections but having the same kinetic energy are actually the same unknowns if the energy discretization is taken as $\Delta E = eF\Delta x$. This approach allows us to calculate mobility by effectively solving the BTE in a single section.

Moreover, since the solution of the BTE in a single section does not imply any connection to the source/drain reservoirs, we enforce the charge conservation in the solution of the BTE as a normalization condition for the unknowns.

VI. MOBILITY SIMULATION RESULTS

In this section, we first validate our transport model against mobility simulation results reported in the literature and then compare simulations with some recent experimental results for GAA and MuGFETs. Finally, we investigate the influence of the shape and area on mobility of the MuGFET devices. All simulations are performed at room temperature and whenever carrier density N_{inv} is quoted in (cm^{-2}), it is obtained by normalizing the linear density in (cm^{-1}) by the length D_0 of the semiconductor cross-section perimeter. The energy barrier Φ_B used in the solution of the Schrödinger equation as well as in the computation of the SR scattering matrix elements is calculated as the difference of the electron affinities χ between semiconductor and oxide whose values

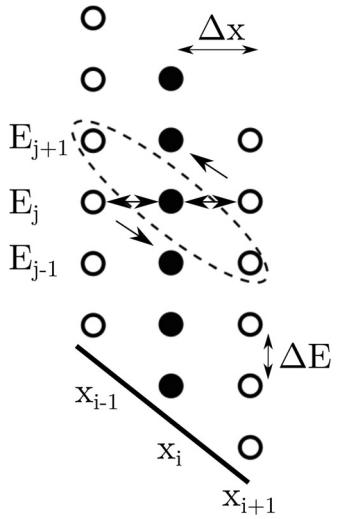

FIG. 6. Schematic view of the unknown distributions in the (x, E_n) space in the case of uniform transport. Points that correspond to the same kinetic energy (see dashed-line oval) have the same occupation function $f_n(x, E_n)$. ΔE and Δx are linked by the electric field $F = \Delta E/\Delta x$. The solid line represents a given subband profile.

TABLE II. Oxide parameters.

HfO_2			ZrO_2			In_2O_3		
$m(\Gamma)^{72}$ (m_0)	χ^{72} (eV)	κ^{73} (ε_0)	$m(\Gamma)^{74}$ (m_0)	χ^{74} (eV)	κ^{73} (ε_0)	$m(\Gamma)^{41}$ (m_0)	χ^{75} (eV)	κ^{41} (ε_0)
0.11	2.0	22	0.30	3.0	24	0.30	3.5	15

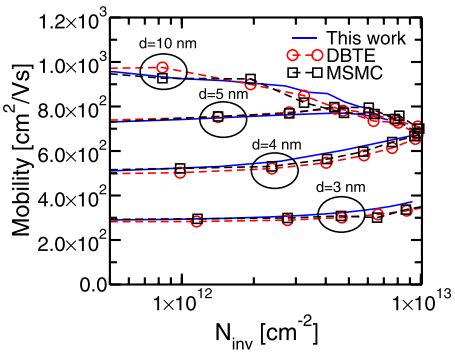

FIG. 7. Simulated phonon-limited mobility for a circular, GAA nanowire with different diameters. The transport direction is [100] and the SiO_2 thickness is 1 nm. Our simulations are compared to DBTE and MSMC results from Ref. 40. Scattering parameters used in these simulations are consistent with Reference 40.

are summarized in Tables I and II, together with a few additional material parameters relevant for our simulations.

A. Validation against previous simulation results

Figure 7 shows a comparison of phonon limited mobility simulations with the results reported in Ref. 40 for cylindrical, silicon GAA-nanowires with [100] transport direction. In order to be consistent with Ref. 40, these simulations have been carried out neglecting the non-parabolicity correction, the electron wave-function penetration into the SiO_2 oxide and the anisotropicity of the silicon Δ-valleys.

A good agreement between our simulations (solid lines) and the results from Ref. 40 (symbols) is observed for different nanowire diameters and over a wide range of N_{inv}.

In order to investigate the effect of non-parabolicity corrections, wave-function penetration into the SiO_2 oxide, and anisotropicity of the silicon Δ-valleys, Fig. 8 shows the phonon-limited mobility obtained under different approximations for two cylindrical GAA devices with diameter $d = 10$ nm and $d = 3$ nm, and using the same scattering parameters as in Fig. 7. As can be seen, the mobility is overestimated when using the simplified model (filled squares) that assumes isotropic, parabolic bands (which underestimate the density of states and scattering rates) and neglects the wave-function penetration in the oxide region. Moreover, with the inclusion of the wave-function penetration into the oxide and non-parabolicity corrections (open circles), simulation results approach quite well the complete model (filled circles), thus revealing that in this case the anisotropy of the energy relation seems to play only a modest role.

B. Comparison with experimental data

In Fig. 9, we present a comparison between simulations and experimental mobility for an InAs cylindrical, GAA FET.[63] Figure 9 also shows the contribution of the different scattering mechanisms by reporting the mobility calculated including only acoustic, polar, and non-polar optical phonons (open circles), then adding SR scattering (open triangles), and finally including also Coulomb scattering induced by fixed oxide charges $N_{fix} = 4 \times 10^{12}\,cm^{-2}$ and $N_{fix} = 8 \times 10^{12}\,cm^{-2}$. The phonon-limited mobility is approximately one order of magnitude larger than the measurements and a fairly good agreement between simulations and experiments at large inversion densities is obtained by adding SR scattering with $\Delta_{rms} = 0.17$ nm and $\Lambda = 1.4$ nm. Mobility simulations with phonon and SR scattering still largely overestimate mobility at small inversion densities, suggesting that additional scattering mechanisms are presumably at work. In order to further address this point, we investigated the role played by the Coulomb scattering with a fixed interface charge N_{fix}; in fact, the experimental device has a negligible channel doping.[63] By

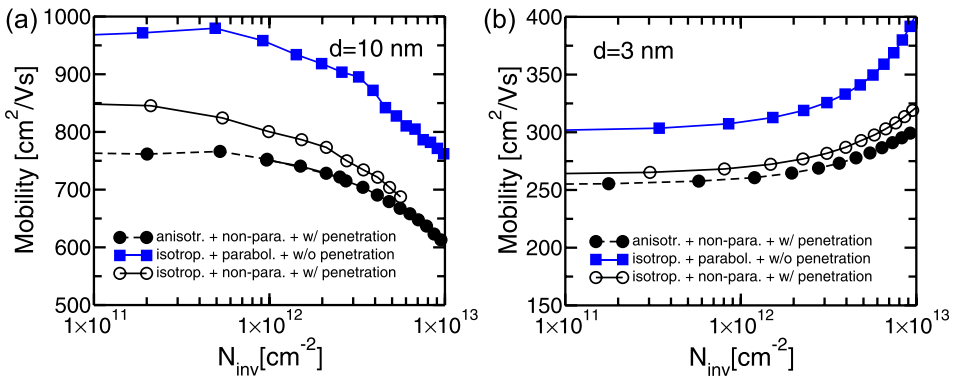

FIG. 8. Simulated phonon-limited mobility for the same device as in Fig. 7 for $d = 3$ nm (right) and $d = 10$ nm (left), and for different modelling approximations. Filled squares: simplified model without band anisotropy, with parabolic bands and without wave-function penetration; empty circles: isotropic bands, with non-parabolicity corrections and wave-function penetration into the oxide; filled circles: complete model with anisotropic bands, valley non-parabolicity and wave-function penetration into the oxide.

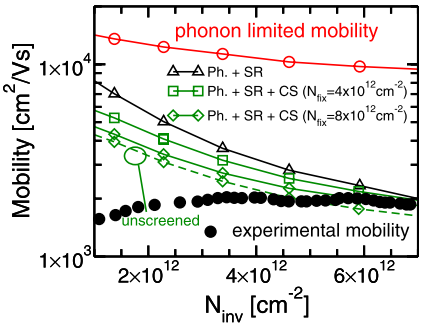

FIG. 9. Mobility simulations (open symbols) obtained for an InAs circular GAA with d = 15 nm and compared with corresponding experiments from Ref. 63 (filled circles). The oxide material is ZrO_2 with a thickness of 4 nm. Simulations have been performed by considering different sets of scattering mechanisms: only phonon scattering (open circles); phonon scattering and SR (open triangles); phonon scattering, SR and CS with $N_{fix} = 4 \times 10^{12}\,cm^{-2}$ (open squares) and $N_{fix} = 8 \times 10^{12}\,cm^{-2}$ (open diamonds). SR parameters are $\Delta_{rms} = 0.17$ nm and $\Lambda = 1.4$ nm. Simulations with SR and CS were also repeated by switching off the carrier screening (dashed line with diamonds).

considering areal densities up to $N_{fix} = 8 \times 10^{12}\,cm^{-2}$, we can improve the agreement with experiments, but simulations still overestimate measured mobility at small N_{inv}. As discussed in more detail in Ref. 64, $N_{fix} = 8 \times 10^{12}\,cm^{-2}$ is probably already too large to be realistic, and a net charge qN_{fix} would induce a shift in I-V curves that is not consistent with experiments, so that we refrained from considering any larger N_{fix} value.

Figure 9 shows that carrier screening plays a modest role in the simulated GAA MOSFET. This almost negligible effect of carrier screening can be explained by noting that, in a degenerate 1D electron gas, intra-subband transitions at energies close to the Fermi level result in a very large exchanged wave-vector $q = (k_x' - k_x)$, which reduces drastically the effect of screening.[35,65] Inter-subband transitions may have a significantly smaller q, but inter-subband screening is weaker.[35,65]

We now move to the mobility simulation of a back-gated (BG), nanowire InAs FET experimentally analyzed in Ref. 66. The simulation domain is sketched in Fig. 10(a), and it includes the thick SiO_2 back-oxide, an In_2O_3 native oxide, and also an air region to mimic the experimental structure and capture capacitive parasitics. The lack of a gate surrounding the cylindrical nanowire breaks the radial symmetry of the wave-function, whose peak is pushed towards the back-oxide, as can be seen in Fig. 10(c) for the wave-function corresponding to the lowest subband; this behavior is expected to influence mobility results. Figure 11 shows the simulated mobility for the BG device reported in Fig. 10(a) compared with experimental results and as a function of the linear electron density, which for experiments has been obtained as $N_{inv} = C_G(V_{GS} - V_T)$, with the capacitance $C_G \simeq 40\,aF/\mu m$ obtained from Fig. 4 of Ref. 66 by extrapolating at a nanowire diameter of 15 nm. Moreover, results for the same nanowire operated in a GAA mode are also shown in Fig. 11 for comparison. A good agreement between simulations and experiments is obtained with a $\Delta_{rms} = 0.55$ nm and $\Lambda = 2.0$ nm and it is interesting to note that these SR spectrum parameters are close to the values measured in III-V

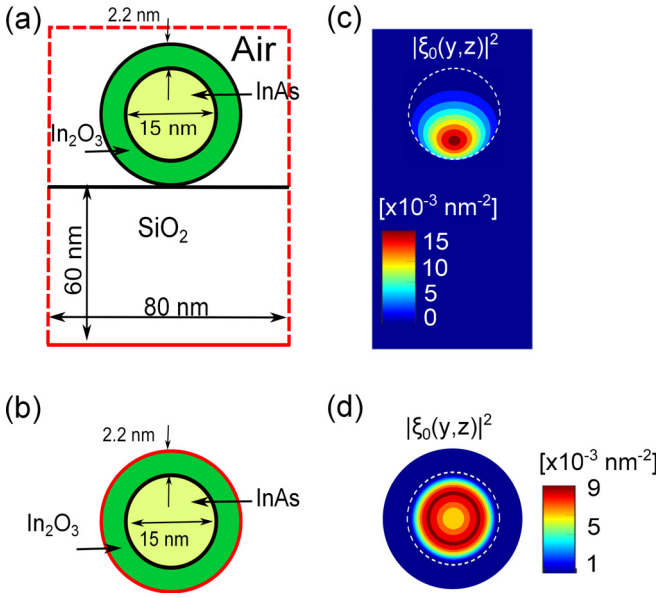

FIG. 10. (a) Simulation domain for the back-gated nanowire. Homogeneous Neumann boundary conditions are imposed in the external domain with dashed lines, whereas Dirichlet boundary conditions are imposed at the bottom of the SiO_2 film (solid line); (b) simulation domain for the same nanowire but with a gate-all-around biasing condition. Squared magnitude of the lowest subband wave-function at $N_{inv} \approx 1 \times 10^7\,cm^{-1}$ for: (c) back-gated nanowire; and (d) gate-all-around nanowire. Reprinted with permission from Badami *et al.*, Tech. Dig. - IEEE Int. Electron Devices Meet. 2016, 36.1.1–36.1.4. Copyright 2017 IEEE.[56]

quantum well FETs.[67] An analysis carried out on the same experimental data but using a linear SR scattering model and GAA biasing conditions, instead, led to a much larger $\Delta_{rms} = 1.2$ nm.[41] The ability of the new, nonlinear SR model to reproduce experiments with substantially smaller and in effect more realistic Δ_{rms} values compared to conventional linear SR models has been already observed and discussed for planar transistors[22,23] and appears to be confirmed in 3D FETs.

We also repeated our simulations using a GAA biasing condition [see Fig. 10(b)] for the same Δ_{rms} and Λ parameters, and Fig. 11 shows that this results in larger mobility values that actually overestimate the experiments. This can be

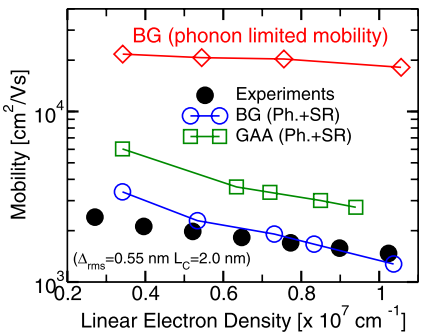

FIG. 11. Mobility versus inversion density N_{inv} in a back-gated (BG), InAs cylindrical FET [open circles, see Fig. 10(a)] with diameter $d = 15$ nm: closed symbols are experiments from Ref. 66; mobility results are also obtained for the same InAs cylindrical FET with gate-all-around (GAA) biasing condition [open squares, see Fig. 10(b)]. Reprinted with permission from Badami *et al.*, Tech. Dig. - IEEE Int. Electron Devices Meet. 2016, 36.1.1–36.1.4. Copyright 2017 IEEE.[56]

explained resorting to the wave-function behavior reported in Figs. 10(c) and 10(d). In fact, in the BG mode the wave-function is more confined towards the interface than it is in GAA mode, which implies larger matrix elements for SR scattering and smaller mobility. These results emphasize the importance of our simulation approach that is able to account for arbitrary cross-sections and biasing conditions.

C. Mobility simulations by varying shape and area of the device cross-section

Figure 12 shows mobility simulations at a fixed N_{inv} for GAA circular and square FETs, for Tri-Gate FinFETs (with aspect ratio H_{fin}/W_{fin} of 2:1), and for different cross-sectional areas ranging from 10 to 50 nm^2. The SR spectrum parameters ($\Delta_{rms} = 0.21$ nm and $\Lambda = 1.4$ nm) are those extracted from a fitting with experimental data for planar devices[23] and are the same for III-V and Si MuGFETs. As shown in Fig. 12(a) at $N_{inv} = 2 \times 10^{12}\,cm^{-2}$ mobility is degraded with decreasing area of the cross-section. This is explained by the fact that, at such relatively small N_{inv}, the electron wave-functions and the electron charge spreads in a large fraction of the cross-section (and the charge is in fact maximum at the center of the MuGFET), so that by shrinking the cross-section the wave-function is pushed toward the semiconductor-oxide interface thus increasing the influence of SR scattering. Figure 12(a) also shows that, for InAs nanowires at $N_{inv} = 2 \times 10^{12}\,cm^{-2}$ and for areas smaller than approximately 20 nm^2, we observe a mobility decrease according to an A^3 power law, the same for all the device cross-sections (circular, square, FinFET-like).

For $N_{inv} = 5 \times 10^{12}\,cm^{-2}$, instead, Fig. 12(b) shows that the modulation of mobility with the cross-sectional area is smaller than in Fig. 12(a); this is because at this N_{inv} the external bias has a strong influence on the shape of the wave-function and on its interaction with the semiconductor-oxide interface, whereas the impact of the cross-sectional area is comparably weaker. Figure 12(b) also shows that the SR is responsible for a strong mobility degradation if we compare mobility results obtained with the inclusion of the SR (solid line with diamonds) and with phonons only (dashed line with diamonds).

Moreover, Fig. 12(b) shows mobility fluctuations versus the cross-sectional area; these are specific of a 1DEG system with large subband separation and are related to the peculiar behavior of the density-of-states and to the relative position of the subbands with respect to the Fermi level. This behavior has already been investigated in III-V MOSFETs[41] and experimentally observed in silicon nanowire MOSFETs at low temperature.[68]

VII. CONCLUSIONS

In this paper, we have developed a nonlinear SR scattering model for GAA MOSFETs and MuGFETs with fairly arbitrary cross-sections and biasing schemes which is a very substantial extension of our previous contribution limited to planar FETs.[22,23] The SR model has been implemented in a mobility simulator that directly solves the BTE without simplifying approximations, and including the effects of anisotropy and non-parabolicity of the energy dispersion relation, as well as the penetration of the wave-function into the oxide region.

The nonlinear SR model is able to reproduce experiments in GAA nanowires with smaller and actually more realistic values of the r.m.s. roughness compared to conventional linear models, thus confirming a trend already observed and discussed in detail for planar MOSFETs.[22,23]

Our results also emphasize the importance of the flexibility in simulation approach when comparing to experimental data, in order to allow for a realistic description of the cross-section of MuGFETs and of the biasing condition, because biasing condition can affect the features of the electron wave-functions and thus influence scattering rates and ultimately mobility.

We have found that free carrier screening plays a modest role in III-V based GAA MOSFETs with strong degeneracy compared, for instance, to III-V transistors realized in a planar architecture, and thus corresponding to a 2D as opposed to a 1D carrier gas. This behaviour is related to the large exchanged momentum in the intra-subband transitions of a 1D electron gas occurring at energies close to the Fermi level. Another feature specific of a 1D gas is a maximum of scattering rates and thus a minimum of mobility for those cross-sectional area and inversion density conditions such that a subband minimum crosses the Fermi level.

In narrow MuGFETs, mobility and transport are thus substantially influenced by the shape of the cross-section, the biasing scheme, and the features of the 1D electron gas induced by carrier confinement, which emphasizes the importance of physically based scattering and transport models as the ones developed and discussed in this paper.

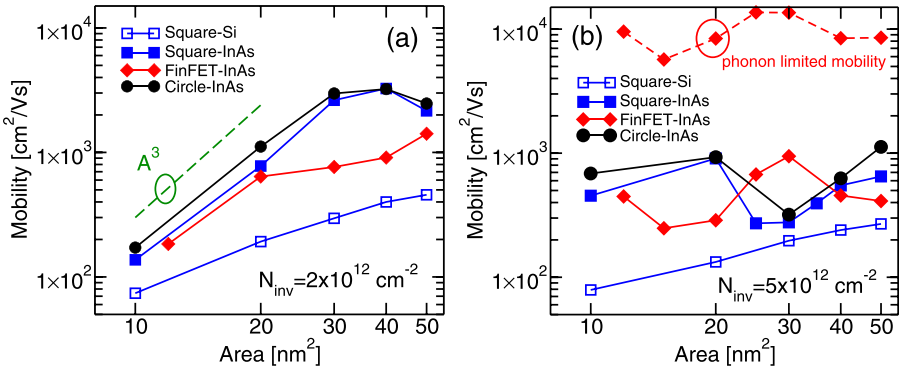

FIG. 12. Simulated mobility versus cross-section area for GAA nanowire MOSFETs with square or circular cross-section and for Tri-Gate FinFET: simulations include phonon and SR scattering with $\Delta_{rms} = 0.21$ nm and $\Lambda = 1.4$ nm. (a) Inversion density $N_{inv} = 2 \times 10^{12}\,cm^{-2}$; (b) $N_{inv} = 5 \times 10^{12}\,cm^{-2}$.

ACKNOWLEDGMENTS

We would like to thank one of the reviewers for helping us make the paper more focused on the original contributions to the modeling of surface roughness scattering, which improved substantially the overall quality of the manuscript.

APPENDIX A: DERIVATION OF THE MATRIX ELEMENT IN EQ. (10)

Before discussing the calculation of the integral over $P_R[\Delta(s, x)]$ in Eq. (7), we introduce a few necessary considerations about the parametrization of the MuGFET cross-section. Let us consider a parametrization $\mathbf{r}(t) = f(t)\hat{\imath}_y + g(t)\hat{\imath}_z$ of the curve $\mathcal{I}_0$ in Fig. 1(a), where $\hat{\imath}_y$ and $\hat{\imath}_z$ are the unit vectors in y and z directions and t is the parameter. From $\mathbf{r}(t)$, we can define the abscissa $s(t)$ along $\mathcal{I}_0$ as

$$s(t) = \int_0^t \left| \frac{d\mathbf{r}(u)}{du} \right| du. \tag{A1}$$

Since $s(t)$ is a positive-defined and monotonically increasing function, there exists a unique inverse function $\tilde{t}(s)$ such that we can write $t = \tilde{t}(s)$; hence, $\mathbf{r}(t)$ can be rewritten in terms of s as $\mathbf{r}(s) = \tilde{f}(s)\hat{\imath}_y + \tilde{g}(s)\hat{\imath}_z$ where $\tilde{f}(s) = f[\tilde{t}(s)]$ and $\tilde{g}(s) = g[\tilde{t}(s)]$.

The unit vector tangent to the curve $\mathcal{I}_0$ is

$$\begin{aligned} \hat{t}(s) &= \frac{d\mathbf{r}(t)/dt}{|d\mathbf{r}(t)/dt|} = \frac{d\mathbf{r}(t)}{dt} \times \left[\frac{ds(t)}{dt}\right]^{-1} = \frac{d\mathbf{r}(s)}{ds} \\ &= \frac{d\tilde{f}(s)}{ds}\hat{\imath}_y + \frac{d\tilde{g}(s)}{ds}\hat{\imath}_z = t_y(s)\hat{\imath}_y + t_z(s)\hat{\imath}_z, \end{aligned} \tag{A2}$$

and the unit vector normal to the curve $\mathcal{I}_0$ reads

$$\hat{n}(s) = -t_z(s)\hat{\imath}_y + t_y(s)\hat{\imath}_z = n_y(s)\hat{\imath}_y + n_z(s)\hat{\imath}_z. \tag{A3}$$

If we now consider a small region close to $\mathcal{I}_0$, such as the $P_R[\Delta(s, x)]$ sketched in Fig. 1(b) and used in Eq. (7), we can define $\mathcal{I}_\eta$ as the curve obtained by moving, at each points along $\mathcal{I}_0$, of a distance η in the direction normal to $\mathcal{I}_0$ identified by $\hat{n}$ (s). The relation that links the coordinates system (y, z) to (s, η) is thus

$$\begin{cases} y = \tilde{f}(s) + \eta\, n_y(s) \\ z = \tilde{g}(s) + \eta\, n_z(s) \end{cases}, \tag{A4}$$

and the Jacobian of the transformation from (y, z) to (s, η) is

$$\begin{aligned} J(s,\eta) &= \det \begin{bmatrix} \frac{\partial y}{\partial s} & \frac{\partial y}{\partial \eta} \\ \frac{\partial z}{\partial s} & \frac{\partial z}{\partial \eta} \end{bmatrix} = \begin{bmatrix} t_y - \eta \frac{\partial t_z}{\partial s} & -t_y \\ t_z + \eta \frac{\partial t_y}{\partial s} & +t_z \end{bmatrix} \\ &= 1 + \eta\left(t_z \frac{\partial t_y}{\partial s} - t_y \frac{\partial t_z}{\partial s}\right), \end{aligned} \tag{A5}$$

where we have used $t_y^2 + t_z^2 = 1$. We notice that $J(s, 0) = 1$, and in fact the length of the curve $\mathcal{I}_0$ is $D_0 = \int_0^{D_0} J(s, 0) ds$.

We now move to the calculation of the integral inside square brackets in Eq. (7), which can be rewritten by using the new integrating variables (s, η) as

$$\begin{aligned} &\iint_{P_R[\Delta(s,x)]} \xi_{n'}^\dagger(\mathbf{r})\, \Phi_B\, \xi_n(\mathbf{r})\, d\mathbf{r} \\ &\quad = \int_0^{D_0} \int_0^{\Delta(s,x)} \xi_{n'}^\dagger(s,\eta)\, \Phi_B\, \xi_n(s,\eta) J(s,\eta)\, d\eta\, ds. \end{aligned} \tag{A6}$$

For small η values (either positive or negative), the Jacobian of the transformation from Cartesian to curvilinear coordinates is now approximated with its average value $\bar{J}(s, \eta)$ along the curve $\mathcal{I}_\eta$, that is

$$\bar{J}(s,\eta) = \frac{\int_0^{D_0} J(s,\eta) ds}{\int_0^{D_0} ds} = \frac{D_\eta}{D_0}. \tag{A7}$$

We now recall that Eq. (8) writes $\xi_n(\mathbf{r})$ as a function of (s_η, η); however, Fig. 1(a) shows that, for each $\mathcal{I}_\eta$, a one-to-one relation must exist between s_η and s that we express as $\tilde{s_\eta}(s)$. Therefore, Eq. (8) can be rewritten as a function of s as

$$\xi_n(\eta, s) = \sum_l \phi_{n,l}(\eta);\, e^{i2\pi l \tilde{s_\eta}(s)/D_\eta}. \tag{A8}$$

Equation (A8) in principle requires to determine $\tilde{s_\eta}(s)$ to proceed further, but in the case of small η values, we can introduce a second approximation by linearizing $\tilde{s_\eta}(s)$ as

$$\tilde{s_\eta}(s) \approx \frac{D_\eta}{D_0} s, \tag{A9}$$

that fulfills the conditions $\tilde{s_\eta}(0) = 0$ and $\tilde{s_\eta}(D_0) = D_\eta$. By substituting Eqs. (A7)–(A9) in Eq. (A6) and then Eq. (A6) back in Eq. (7), we finally obtain Eq. (10) of the main text. We conclude the Appendix by noting that Eqs. (A7) and (A9) are exact for polygonal and circular cross-sections, as well as for cross-sections obtained by any combination of arcs of circles and segments.

[1]The International Technology Roadmap for Semiconductors (ITRS) (2015).
[2]M. Rau, E. Caruso, D. Lizzit, P. Palestri, D. Esseni, A. Schenk, L. Selmi, and M. Luisier, Tech. Dig. - IEEE Int. Electron. Devices Meet. **2016**, 30.6.1–30.6.4.
[3]Y. Q. Wu, R. S. Wang, T. Shen, J. J. Gu, and P. D. Ye, Tech. Dig. - IEEE Int. Electron. Devices Meet. **2009**, 1–4.
[4]K. Tomioka, M. Yoshimura, and T. Fukui, Tech. Dig. - IEEE Int. Electron Devices Meet. **2011**, 33.3.1–33.3.4.
[5]N. Waldron, C. Merckling, L. Teugels, P. Ong, S. A. U. Ibrahim, F. Sebaai, A. Pourghaderi, K. Barla, N. Collaert, and A. V. Y. Thean, IEEE Electron Device Lett. **35**, 1097 (2014).
[6]J. A. D. Alamo, D. A. Antoniadis, J. Lin, W. Lu, A. Vardi, and X. Zhao, IEEE J. Electron Devices Soc. **4**, 205 (2016).
[7]C. B. Zota, F. Lindelow, L.-E. Wernersson, and E. Lind, Tech. Dig. - IEEE Int. Electron Devices Meet. **2016**, 3.2.1–3.2.4.

[8]H. Schmid, D. Cutaia, J. Gooth, S. Wirths, N. Bologna, K. E. Moselund, and H. Riel, Tech. Dig. - IEEE Int. Electron Devices Meet. **2016**, 3.6.1–3.6.4.

[9]R. Xie, P. Montanini, K. Akarvardar, N. Tripathi, B. Haran, S. Johnson, T. Hook, B. Hamieh, D. Corliss, J. Wang, X. Miao, J. Sporre, J. Fronheiser, N. Loubet, M. Sung, S. Sieg, S. Mochizuki, C. Prindle, S. Seo, A. Greene, J. Shearer, A. Labonte, S. Fan, L. Liebmann, R. Chao, A. Arceo, K. Chung, K. Cheon, P. Adusumilli, H. Amanapu, Z. Bi, J. Cha, H.-C. Chen, R. Conti, R. Galatage, O. Gluschenkov, V. Kamineni, K. Kim, C. Lee, F. Lie, Z. Liu, S. Mehta, E. Miller, H. Niimi, C. Niu, C. Park, D. Park, M. Raymond, B. Sahu, M. Sankarapandian, S. Siddiqui, R. Southwick, L. Sun, C. Surisetty, S. Tsai, S. Whang, P. Xu, Y. Xu, C. Yeh, P. Zeitzoff, J. Zhang, J. Li, J. Demarest, J. Arnold, D. Canaperi, D. Dunn, N. Felix, D. Gupta, H. Jagannathan, S. Kanakasabapathy, W. Kleemeier, C. Labelle, M. Mottura, P. Oldiges, S. Skordas, T. Standaert, T. Yamashita, M. Colburn, M. Na, V. Paruchuri, S. Lian, R. Divakaruni, T. Gow, S. Lee, A. Knorr, H. Bu, and M. Khare, Tech. Dig. - IEEE Int. Electron Devices Meet. **2016**, 2.7.1–2.7.4.

[10]D. Bae, G. Bae, K. K. Bhuwalka, S.-H. Lee, M.-G. Song, T. S. Jeon, C. Kim, W. Kim, J. Park, S. Kim, U. Kwon, J. Jeon, K.-J. Nam, S. Lee, S. Lian, K. I. Seo, S.-G. Lee, J. H. Park, Y.-C. Heo, M. S. Rodder, J. A. Kittl, Y. Kim, K. Hwang, D.-W. Kim, M. S. Liang, and E. Jung, Tech. Dig. - IEEE Int. Electron Devices Meet. **2016**, 28.1.1–28.1.4.

[11]Y. J. Lee, T. C. Hong, F. K. Hsueh, P. J. Sung, C. Y. Chen, S. S. Chuang, T. C. Cho, S. Noda, Y. C. Tsou, K. H. Kao, C. T. Wu, T. Y. Yu, Y. L. Jian, C. J. Su, Y. M. Huang, W. H. Huang, B. Y. Chen, M. C. Chen, K. P. Huang, J. Y. Li, M. J. Chen, Y. Li, S. Samukawa, W. F. Wu, G. W. Huang, J. M. Shieh, T. Y. Tseng, T. S. Chao, Y. H. Wang, and W. K. Yeh, Tech. Dig. - IEEE Int. Electron Devices Meet. **2016**, 33.5.1–33.5.4.

[12]K. J. Kuhn, IEEE Trans. Electron Devices **59**, 1813 (2012).

[13]S. Barraud, J. M. Hartmann, V. Maffini-Alvaro, L. Tosti, V. Delaye, and D. Lafond, IEEE Trans. Electron Devices **61**, 953 (2014).

[14]H. Mertens, R. Ritzenthaler, A. Chasin, T. Schram, E. Kunnen, A. Hikavyy, L.-A. Ragnarsson, H. Dekkers, T. Hopf, K. Wostyn, K. Devriendt, S. A. Chew, M. S. Kim, Y. Kikuchi, E. Rosseel, G. Mannaert, S. Kubicek, S. Demuynck, A. Dangol, N. Bosman, J. Geypen, P. Carolan, H. Bender, K. Barla, N. Horiguchi, and D. Mocuta, Tech. Dig. - IEEE Int. Electron Devices Meet. **2016**, 19.7.1–19.7.4.

[15]M. Karner, O. Baumgartner, Z. Stanojević, F. Schanovsky, G. Strof, C. Kernstock, H. Karner, G. Rzepa, and T. Grasser, Tech. Dig. - IEEE Int. Electron Devices Meet. **2016**, 30.7.1–30.7.4.

[16]B. A. Korgel, Nat. Mater. **5**, 521 (2006).

[17]S. D. Suk, M. Li, Y. Y. Yeoh, K. H. Yeo, K. H. Cho, I. K. Ku, H. Cho, W. Jang, D. W. Kim, D. Park, and W. S. Lee, Tech. Dig. - IEEE Int. Electron Devices Meet. **2007**, 891–894.

[18]W. Lu, P. Xie, and C. M. Lieber, IEEE Trans. Electron Devices **55**, 2859 (2008).

[19]S. Kim, M. Luisier, A. Paul, T. B. Boykin, and G. Klimeck, IEEE Trans. Electron Devices **58**, 1371 (2011).

[20]R. G. Hobbs, N. Petkov, and J. D. Holmes, Chem. Mater. **24**, 1975 (2012).

[21]F. Wang, C. Wang, Y. Wang, M. Zhang, Z. Han, S. Yip, L. Shen, N. Han, E. Y. B. Pun, and J. C. Ho, Sci. Rep. **6**, 32910 (2016).

[22]D. Lizzit, D. Esseni, P. Palestri, and L. Selmi, J. Appl. Phys. **116**, 223702 (2014).

[23]O. Badami, E. Caruso, D. Lizzit, P. Osgnach, D. Esseni, P. Palestri, and L. Selmi, IEEE Trans. Electron Devices **63**, 2306 (2016).

[24]R. E. Prange and T.-W. Nee, Phys. Rev. **168**, 779 (1968).

[25]T. Ando, A. B. Fowler, and F. Stern, Rev. Mod. Phys. **54**, 437 (1982).

[26]S. M. Goodnick, D. K. Ferry, C. W. Wilmsen, Z. Liliental, D. Fathy, and O. L. Krivanek, Phys. Rev. B **32**, 8171 (1985).

[27]C. Jungemann, A. Emunds, and W. Engl, Solid State Electron. **36**, 1529 (1993).

[28]M. V. Fischetti and S. E. Laux, Phys. Rev. B **48**, 2244 (1993).

[29]F. Gámiz, J. B. Roldán, J. A. López-Villanueva, P. Cartujo-Cassinello, and J. E. Carceller, J. Appl. Phys. **86**, 6854 (1999).

[30]D. Esseni, IEEE Trans. Electron Devices **51**, 394 (2004).

[31]T. Ishihara, K. Uchida, J. Koga, and S. ichi Takagi, Jpn. J. Appl. Phys., Part 1 **45**, 3125 (2006).

[32]L. Lucci, P. Palestri, D. Esseni, L. Bergagnini, and L. Selmi, IEEE Trans. Electron Devices **54**, 1156 (2007).

[33]S. Jin, M. Fischetti, and T.-W. Tang, IEEE Trans. Electron Devices **54**, 2191 (2007).

[34]S. Jin, M. Fischetti, and T.-W. Tang, J. Appl. Phys. **102**, 083715 (2007).

[35]D. Esseni, P. Palestri, and L. Selmi, *Nanoscale MOS Transistors - Semi-Classical Transport and Applications*, 1st ed. (Cambridge University Press, 2011).

[36]I. M. Tienda-Luna, F. G. Ruiz, A. Godoy, B. Biel, and F. Gámiz, J. Appl. Phys. **110**, 084514 (2011).

[37]M. Poljak, V. Jovanović, D. Grgec, and T. Suligoj, IEEE Trans. Electron Devices **59**, 1636 (2012).

[38]S. Koba, Y. Ishida, R. A. Kubota, Y. Tsuchiya, H. A. Kamakura, N. Mori, and M. Ogawa, Tech. Dig. - IEEE Int. Electron Devices Meet. **2013**, 12.1.1–12.1.4.

[39]Z. Stanojević and H. Kosina, in *Proceedings of the SISPAD* (2013), pp. 352–355.

[40]M. Lenzi, P. Palestri, E. Gnani, S. Reggiani, A. Gnudi, D. Esseni, L. Selmi, and G. Baccarani, IEEE Trans. Electron Devices **55**, 2086 (2008).

[41]E. G. Marin, F. G. Ruiz, A. Godoy, I. M. Tienda-Luna, C. Martínez-Blanque, and F. Gámiz, J. Appl. Phys. **116**, 174505 (2014).

[42]Z. Stanojević, M. Karner, M. Aichhorn, F. Mitterbauer, V. Eyert, C. Kernstock, and H. Kosina, in *Proceedings of the European Solid State Device Research Conference* (2015), pp. 310–313.

[43]A. Paussa, R. Specogna, D. Esseni, and F. Trevisan, J. Comput. Electron. **13**, 287 (2014).

[44]R. Specogna and F. Trevisan, J. Comput. Phys. **230**, 1370 (2011).

[45]J. Wang, A. Rahman, A. Ghosh, G. Klimeck, and M. Lundstrom, IEEE Trans. Electron Devices **52**, 1589 (2005).

[46]Y. Zheng, C. Rivas, R. Lake, K. Alam, T. Boykin, and G. Klimeck, IEEE Trans. Electron Devices **52**, 1097 (2005).

[47]E. Gnani, S. Reggiani, A. Gnudi, P. Parruccini, R. Colle, M. Rudan, and G. Baccarani, IEEE Trans. Electron Devices **54**, 2243 (2007).

[48]F. Stern and W. E. Howard, Phys. Rev. **163**, 816 (1967).

[49]K. Uchida, J. Koga, and S. Takagi, Tech. Dig. - IEEE Int. Electron. Devices Meet. **2003**, 33.5.1–33.5.4.

[50]K. Uchida, M. Saitoh, and S. Kobayashi, Tech. Dig. - IEEE Int. Electron Devices Meet. **2008**, 1–4.

[51]K. Takei, H. Fang, S. B. Kumar, R. Kapadia, Q. Gao, M. Madsen, H. S. Kim, C.-H. Liu, Y.-L. Chueh, E. Plis, S. Krishna, H. A. Bechtel, J. Guo, and A. Javey, Nano Lett. **11**, 5008 (2011).

[52]K. Moors, B. Sorée, and W. Magnus, J. Appl. Phys. **118**, 124307 (2015).

[53]S. Jin, A.-T. Pham, W. Choi, M. Ali Pourhaderi, J. Kim, and K.-H. Lee, in *Proceedings of the SISPAD* **2016**, 109–115.

[54]M. V. Fischetti and S. Narayanan, J. Appl. Phys. **110**, 083713 (2011).

[55]R. Baum, IEEE Trans. Inf. Theory **15**, 448 (1969).

[56]O. Badami, D. Lizzit, R. Specogna, and D. Esseni, Tech. Dig. - IEEE Int. Electron Devices Meet. **2016**, 36.1.1–36.1.4.

[57]M. V. Fischetti and W. G. Vandenberghe, *Advanced Physics of Electron Transport in Semiconductors and Nanostructures* (Springer, 2016).

[58]C. Jacoboni and L. Reggiani, Rev. Mod. Phys. **55**, 645 (1983).

[59]M. Lundstrom, *Fundamentals of Carrier Transport* (Addison Wesley, New York, 1990).

[60]C. Jacoboni, *Theory of Electron Transport in Semiconductors* (Springer-Verlag, Berlin, Heidelberg, 2010).

[61]T. Wang, T. H. Hsieh, and T. W. Chen, J. Appl. Phys. **74**, 426 (1993).

[62]H. U. Baranger and J. W. Wilkins, Phys. Rev. B **36**, 1487 (1987).

[63]T. Vasen, P. Ramvall, A. Afzalian, C. Thelander, K. A. Dick, M. Holland, G. Doornbos, S. W. Wang, R. Oxland, G. Vellianitis, M. J. H. van Dal, B. Duriez, J. R. Ramirez, R. Droopad, L. E. Wernersson, L. Samuelson, T. K. Chen, Y. C. Yeo, and M. Passlack, Tech. Dig. - IEEE Symposium on VLSI Technology **2016**, 1–2.

[64]P. Toniutti, P. Palestri, D. Esseni, F. Driussi, M. D. Michielis, and L. Selmi, J. Appl. Phys. **112**, 034502 (2012).

[65]D. Ferry and S. Goodnick, *Transport in Nanostructures*, Cambridge Studies in Semiconductor Physics and Microelectronic Engineering (Cambridge University Press, 1997).

[66]A. C. Ford, J. C. Ho, Y.-L. Chueh, Y.-C. Tseng, Z. Fan, J. Guo, J. Bokor, and A. Javey, Nano Lett. **9**, 360 (2009).

[67]S. Kim, M. Yokoyama, N. Taoka, R. Iida, S. Lee, R. Nakane, Y. Urabe, N. Miyata, T. Yasuda, H. Yamada, N. Fukuhara, M. Hata, M. Takenaka, and S. Takagi, Appl. Phys. Express **4**, 114201 (2011).
[68]Y. Hironori, M. Naoya, S. Jun, and T. Kimoto, J. Appl. Phys. **106**, 034312 (2009).
[69]I. Vurgaftman, J. R. Meyer, and L. R. Ram-Mohan, J. Appl. Phys. **89**, 5815 (2001).
[70]D. Lizzit, D. Esseni, P. Palestri, P. Osgnach, and L. Selmi, IEEE Trans. Electron Devices **61**, 2027 (2014).
[71]M. V. Fischetti, IEEE Trans. Electron Devices **38**, 634 (1991).
[72]S. Monaghan, P. Hurley, K. Cherkaoui, M. Negara, and A. Schenk, Solid State Electron. **53**, 438 (2009).
[73]M. V. Fischetti, D. A. Neumayer, and E. A. Cartier, J. Appl. Phys. **90**, 4587 (2001).
[74]M. Auf der Maur, M. Povolotskyi, F. Sacconi, A. Pecchia, and A. Di Carlo, J. Comput. Electron. **7**, 398 (2008).
[75]H. Jia, Y. Zhang, X. Chen, J. Shu, X. Luo, Z. Zhang, and D. Yu, Appl. Phys. Lett. **82**, 4146 (2003).